An Investigation on the Effects of Non-Gaussian Noise Transients and Their Mitigations to Tests of General Relativity

Jack Y. L. Kwok*
Department of Physics, The Chinese University of Hong Kong, Shatin, N.T., Hong Kong

Mentors: Alan J. Weinstein, Rico K. L. Lo
LIGO, California Institute of Technology, Pasadena, California 91125, USA

(Dated: December 23, 2020)

The detection of gravitational waves from compact binary coalescence by Advanced LIGO and Advanced Virgo provides an opportunity to study the strong-field, highly-relativistic regime of gravity. Gravitational-wave tests of General Relativity (GR) typically assume Gaussian and stationary detector noise, thus do not account for non-Gaussian, transient noise features (glitches). We present the results obtained by performing parameterized gravitational-wave tests on simulated signals from binary-black-hole coalescence overlapped with three classes of frequently occurring instrumental glitches with distinctly different morphologies. We then review and apply three glitch mitigation methods and evaluate their effect on reducing false deviations from GR. We show that the mitigation methods of inpainting using an inpainting filter and glitch model subtraction using the `BayesWave` algorithm can consistently reduce false violations of GR introduced by these glitches by considering 9 cases of glitches overlapping with signals.

I. INTRODUCTION

Over a century after its formulation in 1915, Einstein's General Relativity (GR) remains as the accepted theory of gravity, passing all precision tests to date [1]. In the weak-field, slow-motion regime, where the effects of metric theories of gravity can be approximated as higher-order *post-Newtonian* (PN) corrections to the Newtonian theory [2], GR lies within the stringent bounds set by solar-system tests and pulsar tests [3, 4]. Recent attention has turned to testing GR in the strong-field, highly-relativistic regime [3], which potentially suggests high-energy corrections to the Einstein-Hilbert action [5], making GR compatible with standard quantum field theory [1]. One approach of probing the strong-field regime is through the detection of gravitational waves (GWs), which propagates at the speed of light and carries information about its astrophysical origin [6].

Of all strong-field astrophysical events that could be probed using GWs, the *coalescence* of stellar-mass binary black holes (BBHs), which can be schematically divided into *inspiral*, *merger* and *ringdown* (IMR) stages, plays a crucial role in testing GR [1]. Since the orbital separation of BBHs can reach far below the last stable orbit before merging, the generated gravitational field can be many order of magnitudes stronger than other astrophysical events observed so far [7–9]. Moreover, GWs emitted by coalescing BBHs offers one of the cleanest test of GR, as matter and electromagnetic fields are negligible for most sources [8, 10], and the emitted GWs essentially propagate through matter unimpeded [8], enabling precision tests of the strong-field dynamics of GR. Since 2015, Advanced LIGO [11] and Advanced Virgo [12] have jointly announced over 40 confident detections of GWs from coalescing BBHs [13, 14].

Several GW tests of GR using coalescing BBHs are developed to test for *generic* deviations from GR without the need for signal models from competing theories of gravity [8]. For example, consistency tests search for excess power in the residual noise after subtracting a best-fit GR waveform [15], or compare the source parameters inferred using only high-frequency data to that inferred using only low-frequency data [15]; parameterized tests introduce parameterized deformations to waveform approximations to GR and infer the extent of deviation using Bayesian parameter estimation [9]. To this date, no evidence for violations of GR has been identified using GWs emitted by coalescing BBHs [16, 17].

Aside from GWs, output from GW detectors is attributed to many independent sources of random noise [18]. Detector noise is typically modeled as stationary and Gaussian in GW data analysis in light of the central limit theorem, and by assuming that noise characteristics remain stationary over observation timescales [19, 20]. However, these assumptions cannot account for transient, non-Gaussian noise features, commonly referred to as *glitches* [21–23], which pose significant problems to GW searches [22] and may bias GW data analysis by violating the noise model. Three glitches from commonly-seen glitch classes during the O3 observing run are shown in Fig. 1.

Many efforts are made to identify and classify glitches [22, 24–28]. Once a glitch is identified, the data containing the glitch can be removed using various mitigation methods [29–33]. The effects of glitches and their mitigations to the inference of source parameters have been studied in the context of glitches similar to that affecting GW170817 [34]. It is of interest to extend the study to parameterized tests of GR, which share the same noise model and parameter estimation techniques but involv-

* Email: jackkwok@link.cuhk.edu.hk

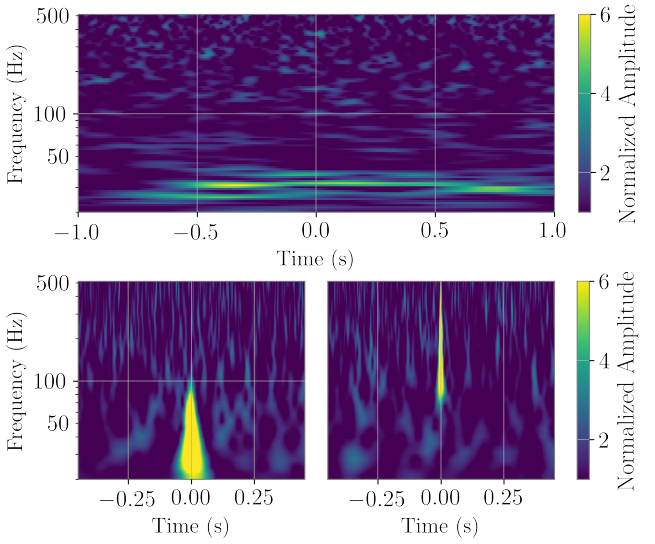

FIG. 1. Glitches with similar morphology can be algorithmically categorized into different classes [22]. A time-frequency representation, called a *Q-scan* (or *Omega scan*) [35], where the duration of each time-frequency bins varies inversely with frequency and linearly with a parameter Q, is commonly used to visualize glitches [22, 28]. Q-scans of three frequently-occurring glitches (top: scattered-light, bottom-left: tomte, bottom-right: blip) during the O3 observing run are shown. The value of Q used is 40, 8 and 8 respectively. The colour represents the normalized amplitude (square root of the normalized power) in each time-frequency bin.

ing extra degree(s) of freedom as parameterized deviations from GR are introduced to the signal model, which may enhance such effects.

This report is structured as follows: Sec. II describes the typical data model used in GW data analyses [19, 20], which composes of a GW signal in additive stationary and Gaussian noise. Sec. III introduces a parameterized test of GR involving the parameterization of the phase of an IMR waveform model [36]. Sec. IV reviews three glitch mitigation methods, namely band-pass filtering, gating and inpainting, and discusses their potential impacts on tests of GR. Sec. V presents the results obtained by performing the parameterized test of GR to glitch-overlapped BBH-coalescence GW signals before and after glitch mitigations.

II. DATA MODEL

A GW detector is designed to respond linearly to the fractional change in arm length, or *strain* [18]. The time series of detector output data $\boldsymbol{d}$, sampled at time t_k at constant sampling interval Δt, can thus be expressed as a linear superposition of a time series of the GW strain signal $\boldsymbol{h}$ and a time series of detector noise $\boldsymbol{n}$:

$$\boldsymbol{d}(t_k) = \boldsymbol{h}(t_k) + \boldsymbol{n}(t_k) \,. \tag{1}$$

In Eq. (1) and in subsequent discussion, boldface denotes the matrix representation of specified quantities.

A. Stationary Gaussian Noise Model

Assuming that a *large* number of independent noise sources contribute linearly to the detector noise $\boldsymbol{n}$, the central limit theorem states that the probability density distribution of the noise $\boldsymbol{n}$ tends to follow a multivariate *Gaussian* distribution [37]:

$$P(\boldsymbol{n}) = \frac{1}{\sqrt{(2\pi)^N |\boldsymbol{\Sigma}|}} e^{-\frac{1}{2}(\boldsymbol{n}-\boldsymbol{\mu})^T \boldsymbol{\Sigma}^{-1} (\boldsymbol{n}-\boldsymbol{\mu})} \,, \tag{2}$$

which is uniquely defined by the *covariance matrix* $\Sigma_{ij} = E[(n(t_i) - \mu(t_i))(n(t_j) - \mu(t_j))]$ and the mean vector $\mu_i = E[n(t_i)]$, where $E[\cdot]$ and $|\cdot|$ denotes the expectation and determinant operation respectively. The diagonal (off-diagonal) terms of the covariance matrix are the variances at each instance of time (correlations between data from different instances of time).

If the number of samples N is large, it is undesirable to invert the $N \times N$ covariance matrix in Eq. (2). Instead, we consider the joint probability density in Fourier domain, which is also a multivariate Gaussian distribution [37]. With the assumption of stationarity, i.e. the joint probability density distribution is time-invariant, the covariance matrix in Fourier domain is diagonalized in the infinite-duration limit [38]. This relation can be approximated for the finite-duration discretely-sampled time series, giving the following approximation to the joint probability density in Fourier domain [38] (for even N), also known as the *Whittle likelihood* [39] in the context of statistical inference:

$$P(\boldsymbol{n}) \simeq \prod_{j=0}^{N/2-1} \frac{2\Delta f}{\pi S_n(f_j)} \exp\left(-\Delta f \frac{2|\tilde{n}_j|^2}{S_n(f_j)}\right) \,, \tag{3}$$

where $f_j \equiv j/N\Delta t$. The quantity $S_n(f_j) \equiv 2|\tilde{n}(f_j)|^2/T$ is scaled from the diagonal terms of the covariance matrix in Fourier domain, $\Delta f \equiv 1/T$ is the *frequency resolution* and the tilde denotes a discrete Fourier transformed (DFT) quantity:

$$\tilde{n}_j \equiv \Delta t \ \mathrm{DFT}[n(t_k)] = \Delta t \sum_{k=0}^{N-1} n(t_k) e^{-2\pi i j k/N} \,. \tag{4}$$

To motivate the quantity $S_n(f_j)$, called the *one-sided power spectral density* (PSD), we invoke Parseval's theorem [38]:

$$\sum_{j=0}^{N/2-1} S_n(f_j)\Delta f \equiv \frac{2}{T} \sum_{j=0}^{N/2-1} |\tilde{n}(f_j)|^2 \Delta f = \frac{1}{N} \sum_{k=0}^{N-1} |n(t_k)|^2 \,, \tag{5}$$

and note that the rightmost side of Eq. (5) returns the *power* of the time series. Since a time series is real, we

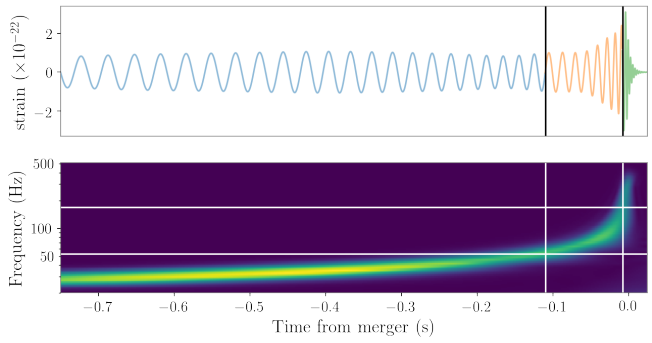

FIG. 2. An example `IMRPhenomPv2` time-domain GW waveform (upper figure) and the corresponding instantaneous frequency (lower figure) plotted against time. The two horizontal lines in the lower figure correspond to the frequencies $0.018/M$ (lower line) and $f_{\rm RD}/2$ (upper line), which defines the boundaries of the inspiral, intermediate and merger-ringdown stages in Fourier domain. The corresponding boundaries in time domain (vertical lines) are determined as the times when the instantaneous frequency of the signal intersects with the Fourier-domain boundaries.

have the property $\tilde{n}(f_j) = \tilde{n}^*(-f_j)$. Consequently, we can sample only the frequency bins from 0 Hz to up to the *Nyquist frequency* $1/2\Delta t$, and introduce the factor of 2 in Eq. (3) and Eq. (5).

B. Signal Model

Since the two-body self-gravitating problem cannot be solved analytically in GR, we generate simulated GW strain signals from coalescing BBHs using the frequency-domain precessing IMR waveform model `IMRPhenomPv2` [36] in virtue of its good match with Numerical Relativity (NR) waveforms [40] and low computational costs.

`IMRPhenomPv2` is a phenomenological waveform model constructed by combining PN-like inspiral waveforms with NR-calibrated merger-ringdown ansatz [41]. Its *inspiral* stage is modeled up to $f \sim 0.018/M$ (in natural units), where M is the total mass of the system. The region with $Mf \geq 0.018$ is subdivided into an *intermediate* stage with $0.018 \geq Mf \geq 0.5 f_{\rm RD}$, which bridges the inspiral stage to the *merger-ringdown* stage modeled above half the ringdown frequency $f_{\rm RD}$ [41]. Fig. 2 illustrates the stages of coalescence of an example `IMRPhenomPv2` GW strain and its frequency evolution over time.

The phase of `IMRPhenomPv2` composes of terms with known frequency dependence. The coefficients of these terms, denoted as the *phase coefficients* p_i, are the subjects of parameterized tests of GR in Section III. The phase coefficients p_i and the orbital evolution of the BBH depend only on the masses and spin angular momentum vectors of the component black holes [40], denoted as the *intrinsic* parameters. The phase coefficients p_i can be categorized into three groups, depending on the stages of coalescence in which they predominantly assert their effect on [9, 41]: (i) the *inspiral* PN coefficients $\{\varphi_0, ..., \varphi_5, \varphi_{5l}, \varphi_6, \varphi_{6l}, \varphi_7\}$ and phenomenological coefficients $\{\sigma_0, ..., \sigma_4\}$; (ii) the *intermediate* phenomenological coefficients $\{\beta_0, ..., \beta_3\}$; (iii) the *merger-ringdown* phenomenological and black hole perturbation theory coefficients $\{\alpha_0, ..., \alpha_5\}$.

Seven additional *extrinsic* parameters, including the sky location, luminosity distance, polarization angle of the source, and the spatial orientation and orbital phase of the system at a reference frequency and time respectively, are needed to determine the response of the GW detectors.

III. PARAMETERIZED TESTS OF GR

We will focus on a parameterized test of GR, which introduces *fractional* deviations δp_i, also known as *dephasing coefficients*, to `IMRPhenomPv2` phase coefficients p_i [9]:

$$p_i \mapsto p_i[1 + \delta p_i] \, . \tag{6}$$

For the exceptional case where $p_i = 0$, such as φ_1, an *absolute* deviation is instead introduced [9]. In practice, we do not allow some of the `IMRPhenomPv2` phase coefficients to deviate from their prescribed values as they have large uncertainties or are degenerate with with other coefficients or physical parameters [9]. We therefore perform tests with the remaining 14 dephasing coefficients, henceforth denoted as the *testing* dephasing coefficients [9]:

$$\{\delta p_i\} = \{\delta\varphi_0, ..., \delta\varphi_4, \delta\varphi_{5l}, \delta\varphi_6, \delta\varphi_{6l}, \delta\varphi_7, \delta\beta_2, \delta\beta_3, \delta\alpha_2, \delta\alpha_3, \delta\alpha_4\} \, .$$

The frequency dependence of the testing parameters δp_i is shown in Table I [15, 42].

To quantify a deviation from GR, we can infer the most probable values of δp_i through Bayesian parameter estimation, as discussed in the following subsection.

A. Parameter Estimation

Recall our data model $\boldsymbol{d} = \boldsymbol{h} + \boldsymbol{n}$. Introducing parameterized phase deviations to the signal $\boldsymbol{h}$, we denote $\boldsymbol{\theta}(\theta, \delta p_i)$ as the parameter vector generating the signal, which consists of the intrinsic and extrinsic parameters generating the `IMRPhenomPv2` waveform, θ, and the testing parameters δp_i. In practice, the testing parameters are introduced *once at a time*, which is expected to capture a deviation from GR present in multiple phase coefficients, while returning narrower credible intervals [15].

Given the detector output $\boldsymbol{d}$ and prior information I, we wish to infer the conditional probability density of $\boldsymbol{\theta}$, referred to as the *posterior*, by invoking Bayes' theorem

$$P(\boldsymbol{\theta}|\boldsymbol{d}, I) = \frac{P(\boldsymbol{d}|\boldsymbol{\theta}, I) \times P(\boldsymbol{\theta}|I)}{P(\boldsymbol{d}|I)} \, , \tag{7}$$

TABLE I. The frequency dependence of `IMRPhenomPv2` testing parameters used in parameterized tests of GR. The table is reproduced from Table 1 of Ref. [15].

Stage of coalescence	δp_i	f-dependence
Inspiral	$\delta\varphi_0$	$f^{-5/3}$
	$\delta\varphi_1$	$f^{-4/3}$
	$\delta\varphi_2$	f^{-1}
	$\delta\varphi_3$	$f^{-2/3}$
	$\delta\varphi_4$	$f^{-1/3}$
	$\delta\varphi_{5l}$	$\log(f)$
	$\delta\varphi_6$	$f^{1/3}$
	$\delta\varphi_{6l}$	$f^{1/3}\log(f)$
	$\delta\varphi_7$	$f^{2/3}$
Intermediate	$\delta\beta_2$	$\log f$
	$\delta\beta_3$	f^{-3}
Merger-Ringdown	$\delta\alpha_2$	f^{-1}
	$\delta\alpha_3$	$f^{3/4}$
	$\delta\alpha_4$	$\tan^{-1}(af+b)$

which relates the posterior to three probability densities: the *likelihood* $P(\boldsymbol{d}|\boldsymbol{\theta}, I)$, the *prior* $P(\boldsymbol{\theta}|I)$ and the *evidence* $P(\boldsymbol{d}|I)$. During parameter estimation, the evidence, which do not depend explicitly on $\boldsymbol{\theta}$, can be seen as a proportionality constant since $\boldsymbol{d}$ and I are kept fixed. The likelihood and prior is separately discussed below.

Given $\boldsymbol{h}(\boldsymbol{\theta})$, the time series of the output data $\boldsymbol{d}$ uniquely defines a time series of the residual noise $\boldsymbol{d}-\boldsymbol{h}$, which is modeled as Gaussian and stationary. As such, the likelihood is approximated by the Whittle likelihood in Eq. (3):

$$P(\boldsymbol{d}|\boldsymbol{\theta}, I) \propto \exp\left[-\frac{1}{2}(\boldsymbol{d}-\boldsymbol{h}|\boldsymbol{d}-\boldsymbol{h})\right] , \tag{8}$$

where $(\cdot|\cdot)$ is the *noise-weighted inner product* [43]:

$$(\mathbf{a}|\mathbf{b}) \equiv \sum_{j=0}^{N/2-1} 4\Re\left(\frac{\tilde{a}_j^* \tilde{b}_j}{S_n(f_j)}\right)\Delta f . \tag{9}$$

Assuming that noise from multiple detectors, indexed l, are uncorrelated, the joint likelihood takes the form

$$P(\boldsymbol{d}_l|\boldsymbol{\theta}, I) \propto \exp\left[-\frac{1}{2}\sum_l (\boldsymbol{d}_l-\boldsymbol{h}_l|\boldsymbol{d}_l-\boldsymbol{h}_l)\right] . \tag{10}$$

The prior $P(\boldsymbol{\theta}|I)$ incorporates our beliefs about $\boldsymbol{\theta}$ prior to the observation. We follow the default choice of prior in `LALInference` [20], which include uniform priors for the component masses m_1 and m_2, with $m_2 \leq m_1$, a log-uniform prior for the luminosity distance, an isotropic prior for the sky location of the source and the spin angular momentum vectors of the component black holes, and uniform priors for the remaining parameters. We note that in `LALInference`, the uniform priors specified for component masses are transformed to non-uniform, correlated priors for the chirp mass $\mathcal{M} \equiv (m_1 m_2)^{3/5}(m_1+m_2)^{-1/5}$ and the mass ratio $q \equiv m_2/m_1$ for more efficient sampling [20].

In parameterized tests of GR, parameters of primary interest are the testing parameters δp_i, while the posterior distribution spans the full 16-dimensional parameter space. We therefore compute the *marginalized* posterior distribution for introduced the testing parameter δp_i:

$$P(\delta p_i|\boldsymbol{d}, I) = \int P(\boldsymbol{\theta}|\boldsymbol{d}, I) d\theta , \tag{11}$$

where θ denotes the parameters generating the underlying `IMRPhenomPv2` waveform.

IV. GLITCH MITIGATION METHODS

In this section, we review four methods to mitigate data containing glitches, including one frequency-domain filtering method of band-pass filtering, two time-domain filtering method of gating and inpainting, and a glitch model subtraction method using the `BayesWave` method. Out of the four discussed methods, we perform band-pass filtering, inpainting and glitch model subtraction in our study.

A. Band-pass filtering in Frequency Domain

Assuming stationary and Gaussian noise, components of the noise-weighted inner product from different frequency bins of equal bandwidth and from different detectors contribute linearly to the log likelihood, as seen from Eq. (10). A direct way of removing the glitch in Fourier domain is by excluding the frequency bins containing the glitch from the likelihood calculation. In `LALInference`, this can be done by specifying the high-pass and low-pass cutoff frequency for the affected detector such that data containing the glitch is filtered out. Only the passed frequency bins are considered in the likelihood calculation. By default, data is high-passed at 20 Hz in `LALInference` [20].

B. Gating and Inpainting in Time Domain

A similar procedure can be done in the time domain, commonly known as *gating*, in which data containing the glitch is zeroed out by multiplying an inverse window function. The inverse window function reduces the spectral leakage in Fourier domain due to discontinuity of data at the boundary of the region to be zeroed out [44].

Gating is adopted in the mitigation of glitch-overlapped GW170817 signal in LIGO-Livingston during the rapid localization of the source [45], illustrated in Fig.

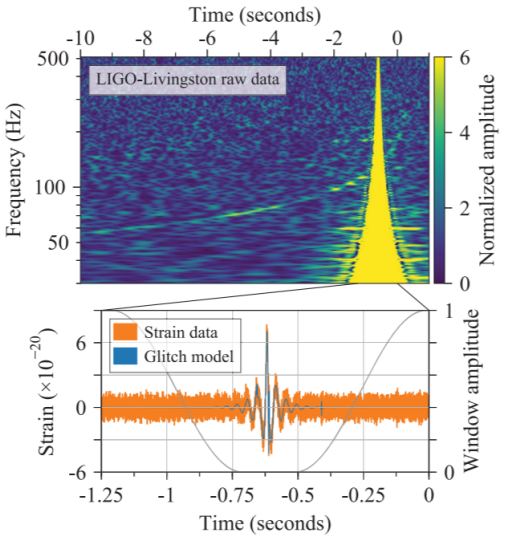

FIG. 3. The output data from LIGO-Livingston for GW170817 is plotted over time in the bottom figure (orange curve). A glitch was identified around the time $t = -0.75$ s to -0.5 s in the figure. To infer the sky location of the event during rapid localization, data was multiplied by an inverse Tukey window function (black curve) [45]. To infer the source properties during parameter estimation, a glitch model (blue curve) reconstructed with `BayesWave` [31, 32] is subtracted from the data [45], which is currently not included in our study. The upper figure shows a spectrogram of the raw LIGO-Livingston data. The figure is retrieved from Abbott et al. [45]

3, which successfully led to follow-up electromagnetic observations [46]. However, gating was not a recommended glitch mitigation method for parameter estimation purposes for the first half of the O3 observing run (O3a) [47]. Some of the concerns and limitations of mitigating glitches by gating are discussed below.

As remarked in Ref. [34], gating can introduce errors to parameterized tests of GR, as it affects the signal power in frequency bins that count towards the noise-weighed inner product. For short-duration glitches, the minimal duration of window is further limited by the spectral leakage in time and frequency domain would be resulted if the window duration is shorter than the inverse width of the spectral line, producing high-amplitude glitch-like noise artifacts at the boundaries in time domain [33].

A new method, called *impainting* or *hole filling* [33], is developed to address the noise artifacts and statistical bias that may be resulted from gating. After specifying the time interval to be mitigated, new values are assigned for data within the interval, or *hole*, according to an *inpainting filter*, while data outside the hole are unaffected. The inpainting filter depends on the PSD of the stationary Gaussian noise. Inpainted data within the hole is identically zero upon twice-whitening by the same PSD, and the quantity $(\boldsymbol{d}|\boldsymbol{h})$ is independent of the template waveform $\boldsymbol{h}$ inside the interval [33]. Since the hole can be made arbitrarily narrow, inpainting affect the minimal amount of data if the glitch is localized in time.

If the PSD used in the inpainting filter equals the PSD estimation used in the likelihood calculation, inpainting is not expected to bias parameterized tests of GR: re-expressing the noise-weighed inner product in the likelihood calculation:

$$P(\boldsymbol{d}|\boldsymbol{h}) \propto \exp\left[-\frac{1}{2}(\boldsymbol{d}-\boldsymbol{h}|\boldsymbol{d}-\boldsymbol{h})\right] = \exp\left[-\frac{1}{2}(\boldsymbol{d}|\boldsymbol{d}) + (\boldsymbol{d}|\boldsymbol{h}) - \frac{1}{2}(\boldsymbol{h}|\boldsymbol{h})\right] . \quad (12)$$

Given inpainted data $\boldsymbol{d}$, only the terms $(\boldsymbol{d}|\boldsymbol{h})$ and $(\boldsymbol{h}|\boldsymbol{h})$ differ across waveform templates $\boldsymbol{h}$; between these two terms, only $(\boldsymbol{d}|\boldsymbol{h})$ explicitly depends on the inpainted data. As $(\boldsymbol{d}|\boldsymbol{h})$ is independent of the template waveform inside the hole, inpainted data inside the hole is not expected to contribute to the outcome of parameterized tests. The desirable behaviors of the inpainting filter may not hold if different estimates of the PSD are used in the inpainting filter and the likelihood calculation. The sensitivity of the inpainting filter towards the PSD deserves a study [48].

C. Glitch Model Subtraction

The `BayesWave` [31, 32] algorithm models the GW signal and glitches in each detector using a variable number of wavelets, such as sine-Gaussian wavelets. Using Bayesian inference and the data model

$$\boldsymbol{d} = \boldsymbol{h} + \boldsymbol{n}_G + \boldsymbol{g} , \quad (13)$$

where the output data in each detector is modeled as a superposition of a GW signal $\boldsymbol{h}$, stationary Gaussian noise $\boldsymbol{n}_G$ and glitches $\boldsymbol{g}$. While both the GW signal and glitches are non-stationary and non-Gaussian, coherent features across data from multiple detectors will be modeled by the signal model and independent features will be modeled by the glitch model [49]. A trans-dimensional Reversible Jump Markov Chain Monte Carlo algorithm is used to sample models with different number of wavelets or with wavelets of different parameter values. The most probable model is inferred through Bayesian inference by comparing the evidence $P(\boldsymbol{d}|M_i, I)$ for different models M_i: given data $\boldsymbol{d}$ and prior information I, we define the *odds* O_2^1 between two competing models M_1, M_2 and invoking Bayes' Theorem

$$O_2^1 \equiv \frac{P(M_1|\boldsymbol{d}, I)}{P(M_2\boldsymbol{d}, I)} = \frac{P(M_1|I)}{P(M_2|I)} \times \frac{P(\boldsymbol{d}|M_1, I)}{P(\boldsymbol{d}|M_2, I)} , \quad (14)$$

we get that model M_1 will be more probable than model M_2 if the odds O_2^1 is larger than 1. Setting the first term on the rightmost of Eq. (14), called the *prior odds*, to unity to express our ignorance towards the probability of models, the odds can be obtained by comparing the

TABLE II. Key specifications of the three mitigation methods.

Mitigation Method	Specification	**Scattered-Light**	**Tomte**	**Blip**
Band-pass	High-pass Cutoff (Hz)	40	105	20
	Low-pass Cutoff (Hz)	511.875	511.875	60
Inpainting	Hole Duration (s)	1.750	0.040	0.005
	Sampling Rate (Hz)	4096	4096	4096
Glitch Model	Segment Length (s)	16	4	4
Subtraction	High-pass Cutoff (Hz)	8	20	20
	Sampling Rate (Hz)	2048	2048	2048
	$Q_{\max}$	200	40	40
	$D_{\max}$	200	100	100

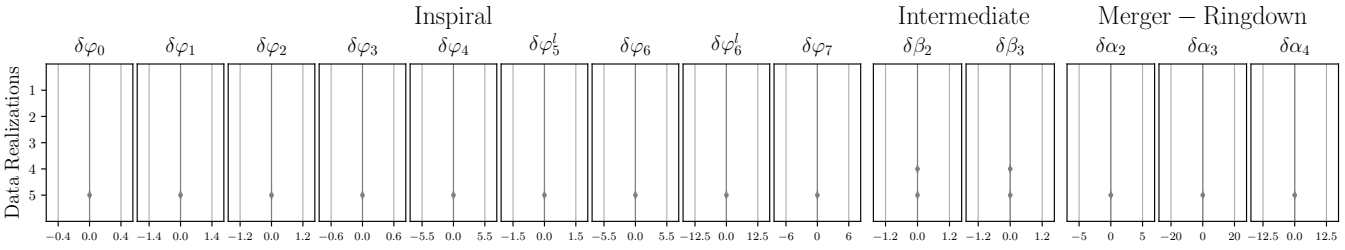

FIG. 4. 90% credible intervals of the posterior distributions of testing parameters obtained by performing parameterized tests of GR on 5 data realizations of a simulated GW190828_065509-like signal in stationary Gaussian noise. The simulated noise is colored by the representative best LIGO-Hanford, LIGO-Livingston and Virgo detector PSD estimates during O3a.

evidences of the two models. In `BayesWave`, the evidences are calculated through thermodynamic integration [31]. Once the most probable glitch+signal model is inferred, the glitch model is subtracted from the data.

The `BayesWave` algorithm was first used to remove the glitch which overlapped with the GW170817 signal during parameter estimation [45], illustrated in Fig. 3, and was regularly used to mitigate glitch-overlapped signals during O3a [14]. Ref. [34] concluded that parameter recovery results using data reconstructed by `BayesWave` are unbiased. In the context of tests of GR, which are designed to detect small deviations from GR waveforms, the subtraction of sine-Gaussian wavelets by `BayesWave` may alter the GW signal to an extent which may be reported as a false violation of GR. However, this is not observed in our results.

V. RESULTS OF GLITCHES OVERLAPPING A GW190828_065509-LIKE SIGNAL

We are motivated to consider a signal similar to that of the high-mass-ratio BBH-merger event GW190828_065509 [14], in which the mitigation of potential glitches overlapping the event in L1 through band-pass filtering resulted in pathological features in parameterized tests of GR [50]. Values of some selected generating parameters of the GW190828_065509-like signal is tabulated in Table III.

TABLE III. Injected values of some selected generating parameters of a GW190828_065509-like signal using the `IMRPhenomPv2` waveform model. The GW190828_065509-like signal is taken to be the *maximum likelihood* waveform inferred for real GW190828_065509 data using the `IMRPhenomPv2` template waveform model. Due to the high mass ratio and strong spins of the GW190828_065509-like signal, precession effects are significant.

Waveform Parameter	Value
Chirp mass $\mathcal{M}$ ($M_\odot$)	16.86
Mass ratio q	0.14
Dimensionless primary spin magnitude a_1	0.92
Dimensionless secondary spin magnitude a_2	0.75
Right ascension α (rad)	2.54
Declination δ (rad)	-0.84

We first present the expected results of parameterized tests of GR in the absence of glitches by coherently injecting the simulated GW190828_065509-like signal, generated with a `IMRPhenomPv2` waveform model, into 5 realizations of simulated stationary, Gaussian noise colored with the representative best (cleaned) PSD of the LIGO-Hanford (H1), LIGO-Livingston (L1) and Virgo (V1) detectors during O3a. The 90% credible intervals for the

testing parameters are plotted in Fig. 4, X a remark on results.

The same signal is then injected into real H1, L1 and V1 detector data [51] at times where glitches are present in either H1 or L1 with all three detectors operating in the science mode. Glitches from the *tomte*, *blip*, *scattered-light* classes (and *fast-scattering* class, which is considered here as a sub-class of the scattered-light class) are chosen, as glitches from these classes have the highest occurrence rates in the first half of the O3 observing run. The glitches used in our study is further chosen so that their duration and peak frequency are representative of their corresponding glitch classes.

For long-duration glitches from the scattered-light class, the GW190828_065509-like signal was injected near the time when the glitch is loudest. For short-duration glitches from the tomte and blip class, the signal was injected coherently into the three detectors such that each glitch overlaps with the signal at the inspiral, intermediate and merger-ringdown stage in time domain in different data samples. The three stages in time domain are determined as the time intervals when the instantaneous frequencies of the signal are in the corresponding three stages in frequency-domain discusseded in Sec. II B respectively. The boundaries of the three stages of the signal in time and frequency domain are marked in the Q-scans by vertical and horizontal white lines respectively.

After preparing the data samples, we applied the glitch mitigation methods of band-pass filtering, inpainting and `BayesWave` glitch subtraction as described in Sec. IV on detector data in which glitches are present. We then performed parameterized tests of GR on the unmitigated and mitigated samples. The specifications of the three glitch mitigation methods are tabulated in Table II.

A. Scattered-light Glitches

Scattered-light glitches are produced by laser light scattering out and re-entering the main laser beam, and their correlation with seismic motion are well-understood [14]. Scattered-light glitches are characterized by their arch shape as seen in a time-frequency representation such as the top Q-scan in Fig. 1 [22]. The simulated GW190828_065509-like signal is coherently injected into H1, L1 and V1 at GPS times around 1253416025, 1253200434 and 1253275979, corresponding to the time when scattered-light glitches are present in H1, L1 and L1 (more precisely, the last one is classified as a fast-scattering glitch by the *Gravity Spy* pipeline [22]). Parameterized tests of GR are performed on the unmitigated and mitigated data, the posterior of the testing parameters are plotted on the left and right side of each violin plot in Fig. 5 respectively. Implications.

Lorem ipsum dolor sit amet, consectetuer adipiscing elit. Ut purus elit, vestibulum ut, placerat ac, adipiscing vitae, felis. Curabitur dictum gravida mauris. Nam arcu libero, nonummy eget, consectetuer id, vulputate a, magna. Donec vehicula augue eu neque. Pellentesque habitant morbi tristique senectus et netus et malesuada fames ac turpis egestas. Mauris ut leo. Cras viverra metus rhoncus sem. Nulla et lectus vestibulum urna fringilla ultrices. Phasellus eu tellus sit amet tortor gravida placerat. Integer sapien est, iaculis in, pretium quis, viverra ac, nunc. Praesent eget sem vel leo ultrices bibendum. Aenean faucibus. Morbi dolor nulla, malesuada eu, pulvinar at, mollis ac, nulla. Curabitur auctor semper nulla. Donec varius orci eget risus. Duis nibh mi, congue eu, accumsan eleifend, sagittis quis, diam. Duis eget orci sit amet orci dignissim rutrum.

Nam dui ligula, fringilla a, euismod sodales, sollicitudin vel, wisi. Morbi auctor lorem non justo. Nam lacus libero, pretium at, lobortis vitae, ultricies et, tellus. Donec aliquet, tortor sed accumsan bibendum, erat ligula aliquet magna, vitae ornare odio metus a mi. Morbi ac orci et nisl hendrerit mollis. Suspendisse ut massa. Cras nec ante. Pellentesque a nulla. Cum sociis natoque penatibus et magnis dis parturient montes, nascetur ridiculus mus. Aliquam tincidunt urna. Nulla ullamcorper vestibulum turpis. Pellentesque cursus luctus mauris.

Nulla malesuada porttitor diam. Donec felis erat, congue non, volutpat at, tincidunt tristique, libero. Vivamus viverra fermentum felis. Donec nonummy pellentesque ante. Phasellus adipiscing semper elit. Proin fermentum massa ac quam. Sed diam turpis, molestie vitae, placerat a, molestie nec, leo. Maecenas lacinia. Nam ipsum ligula, eleifend at, accumsan nec, suscipit a, ipsum. Morbi blandit ligula feugiat magna. Nunc eleifend consequat lorem. Sed lacinia nulla vitae enim. Pellentesque tincidunt purus vel magna. Integer non enim. Praesent euismod nunc eu purus. Donec bibendum quam in tellus. Nullam cursus pulvinar lectus. Donec et mi. Nam vulputate metus eu enim. Vestibulum pellentesque felis eu massa.

B. Tomte Glitch

Tomte glitches are short-duration, broadband glitches characterized by their triangular shape as seen in time-frequency representations. A Q-scan of a tomte glitch is shown on the bottom-left of Fig. 1. The sources and coupling of tomte glitches are not well-understood. The simulated GW190828_065509-like signal is coherently injected into H1, L1 and V1 at GPS times around 1252901859, corresponding to the time when a tomte glitch is present in L1. The injection time is slightly adjusted so that the glitch overlap with the signal at the inspiral, intermediate and merger-ringdown stages in time domain. Parameterized tests of GR are performed on the unmitigated and mitigated data, the posterior of the testing parameters are plotted on the left and right side of each violin plot in Fig. 6 respectively.

Despite shifting the simulated signal to overlap with the tomte glitch at different stages in time domain, similar posterior distributions of testing parameters are ob-

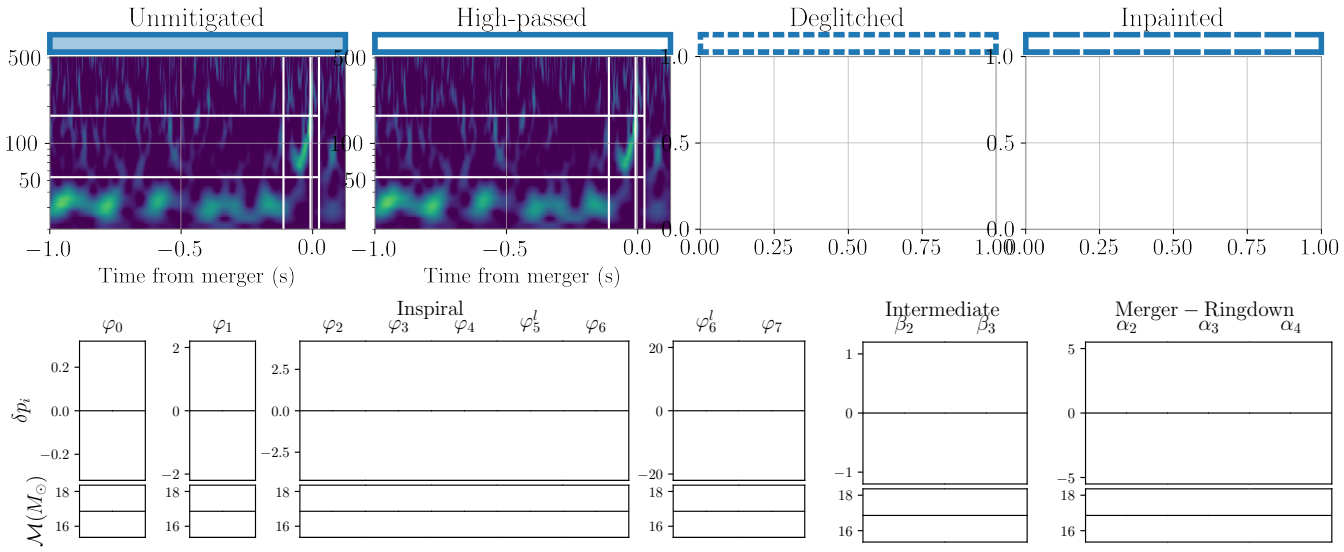

(a) Simulated GW190828_065509-like signal overlapped with a H1 scattered-light glitch.

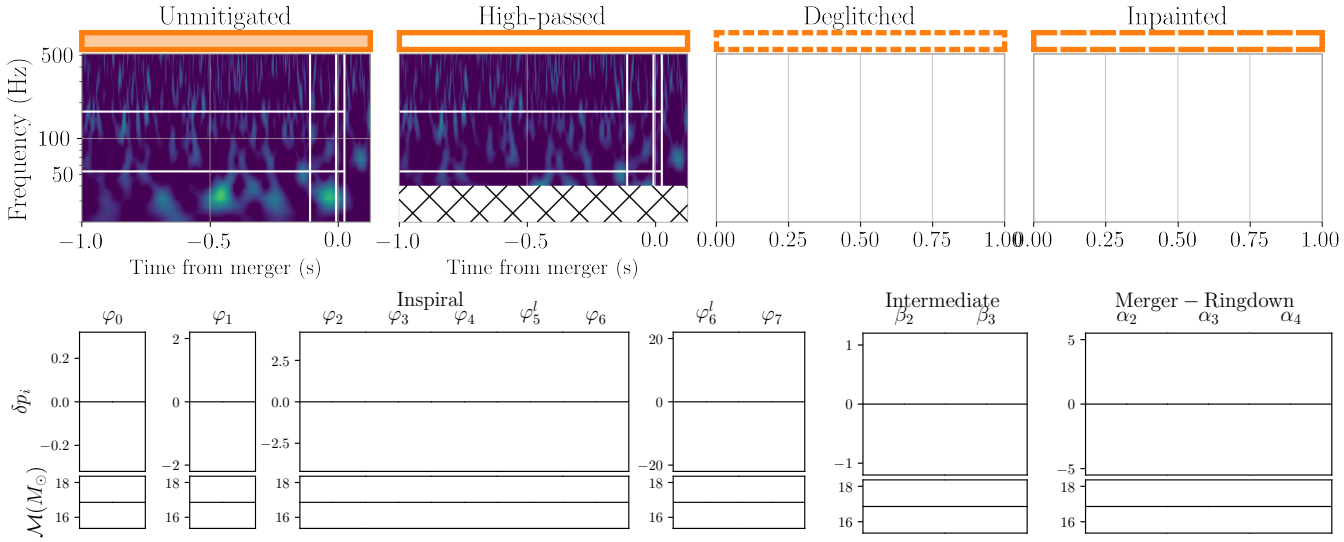

(b) Simulated GW190828_065509-like signal overlapped with a L1 scattered-light glitch.

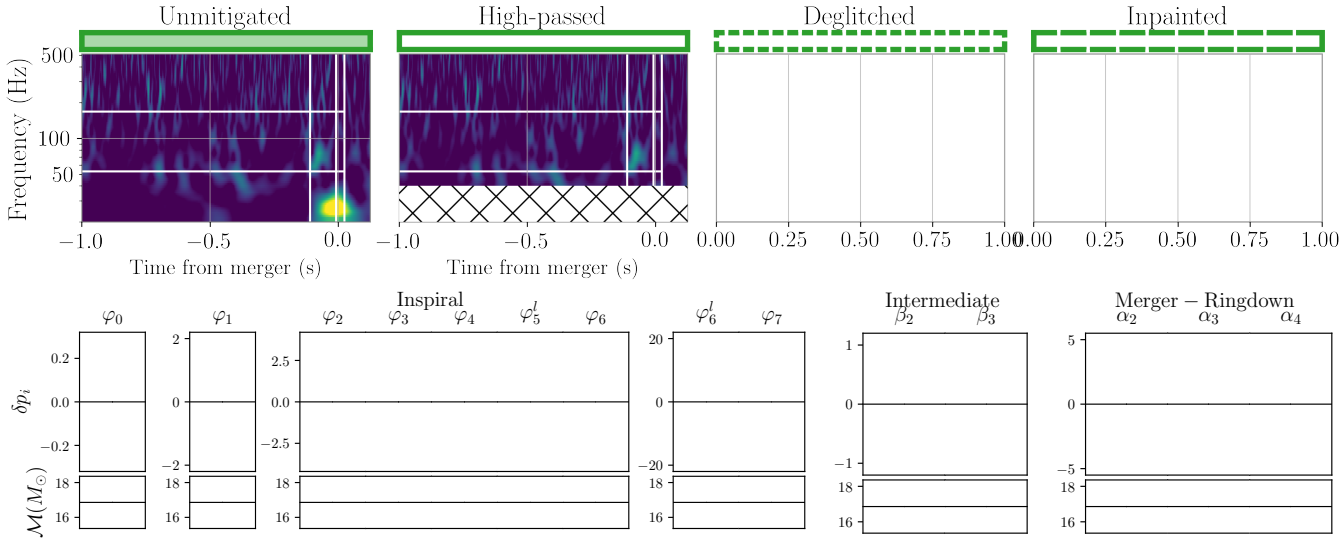

(c) Simulated GW190828_065509-like signal overlapped with a L1 fast-scattering glitch.

FIG. 5. Posterior distributions of testing parameters and the recovered chirp mass obtained by performing parameterized tests on unmitigated scattered-light-glitch-overlapped signals during a three-detector observation (left of violin plot) and the corresponding mitigated cases (right of violin plot) where band-pass filtering (solid line), `BayesWave` glitch model subtraction (dotted line) and inpainting (dashed line) are performed. The GR-value of the testing parameters and the injected value of chirp mass are indicated by vertical black lines.

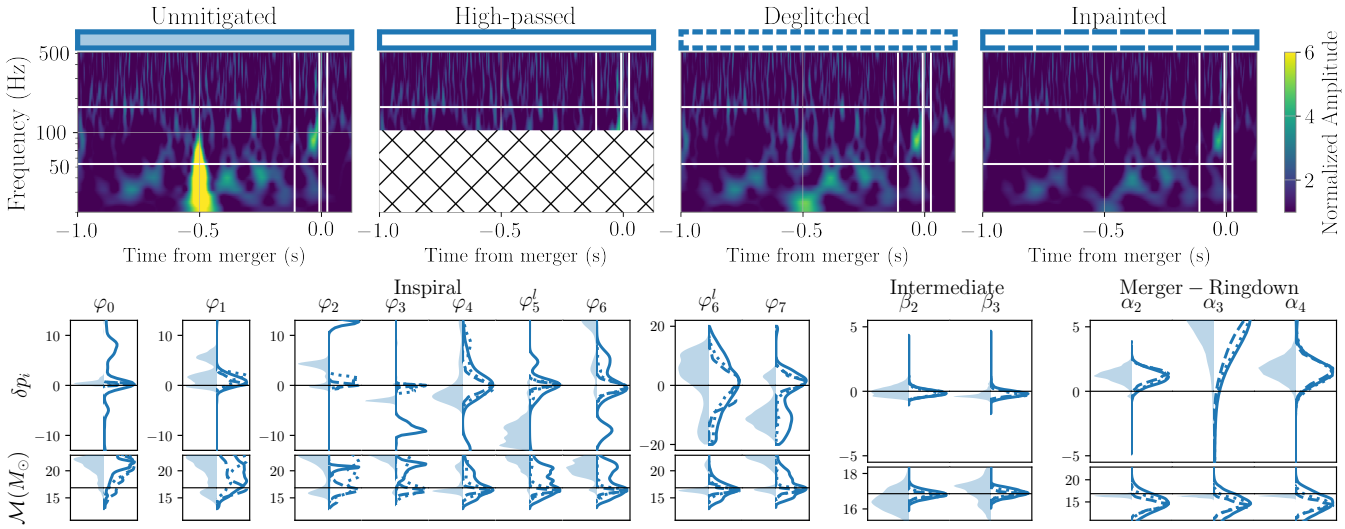

(a) Simulated GW190828_065509-like signal overlapped with a L1 tomte glitch at inspiral stage in time domain.

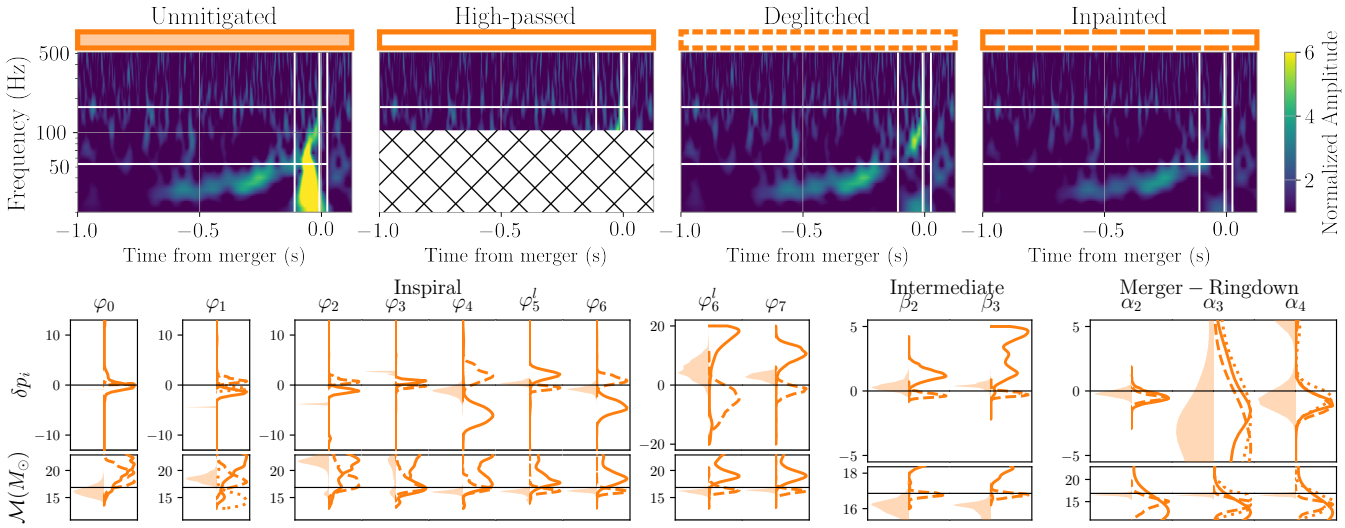

(b) Simulated GW190828_065509-like signal overlapped with a L1 tomte glitch at intermediate stage in time domain.

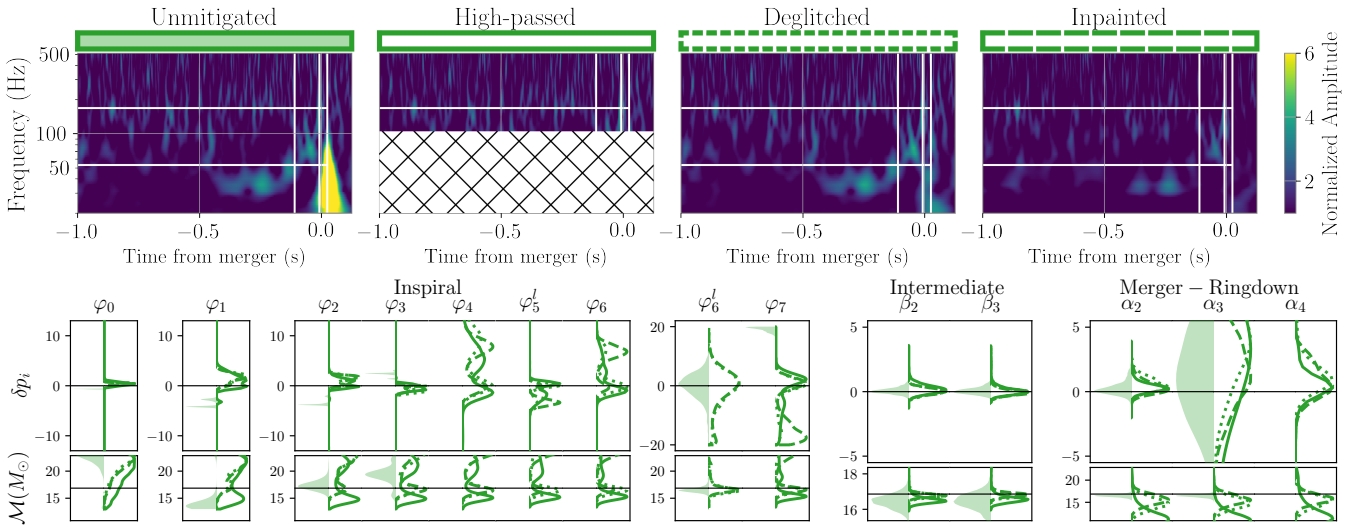

(c) Simulated GW190828_065509-like signal overlapped with a L1 tomte glitch at merger-ringdown stage in time domain.

FIG. 6. Posterior distributions of testing parameters and the recovered chirp mass obtained by performing parameterized tests on unmitigated tomte-glitch-overlapped signals during a three-detector observation (left of violin plot) and the corresponding mitigated cases (right of violin plot) where band-pass filtering (solid line), `BayesWave` glitch model subtraction (dotted line) and inpainting (dashed line) are performed. The GR-value of the testing parameters and the injected value of chirp mass are indicated by vertical black lines.

tained for the three unmitigated cases. Exclusions of the GR value of 0 is clearly observed in lower PN orders, such as $\delta\chi_2$ and $\delta\chi_3$. With the constraint of GR relaxed. The sampling of the chirp mass can be inaccurate when the glitch is present, resulting in multimodal peaks or peaking far away from the injected value, as observed when parameterized deviations are introduced in the inspiral stage. Although the tomte glitch contributes considerable excess power in the intermediate stage in frequency domain, which resides in the most sensitive frequency bands of the LIGO detectors [9], false deviations in the intermediate testing parameters cannot be observed.

Comparing the unmitigated and mitigated results, both inpainting and deglitching can consistently reduce the false violations in the lower PN order testing parameters, resulting in strong support for the GR value of 0 in most testing parameters. Meanwhile, high-passing up to 105 Hz is not a robust glitch mitigation method, as false deviations of GR can be amplified (e.g. $\delta\chi_2, \delta\chi_3$ in Fig. 6a) or introduced by the mitigation (e.g. $\delta\beta_2, \delta\beta_3$ in Fig. 6b). Improvement in parameterized tests of GR upon removal of the glitch suggests that the false violations in the inspiral parameters are attributed to the presence of the tomte glitch, which contributes significant excess power in inspiral frequency bands. Despite the effectiveness of inpainting and deglitching in reducing false deviations of GR, the sampling of intrinsic parameters such as chirp mass can still be difficult when parameterized deviations are introduced (e.g. multimodal peaks resulted for inpainted and deglitched data when $\delta\chi_2, \delta\chi_3, \delta\chi_4, \delta\chi_5^l$ are introduced in Fig. 6c).

C. Blip Glitch

Blip glitches are short-duration, broadband glitches characterized by their teardrop shape as seen in time-frequency representations. A Q-scan of a blip glitch is shown on the bottom-right of Fig. 1 [22]. The sources and coupling of blip glitches are not well-understood [14]. The simulated GW190828_065509-like signal is coherently injected into H1, L1 and V1 at GPS times around 1253103382.105, corresponding to the time when a blip glitch is present in H1. The injection time is slightly adjusted so that the glitch overlap with the signal at the inspiral, intermediate and merger-ringdown stages in time domain. Parameterized tests of GR are performed on the unmitigated and mitigated data, the posterior of the testing parameters are plotted on the left and right side of each violin plot in Fig. 7 respectively.

Violations of GR can be observed for testing parameters from all stages of coalescence when the blip glitch overlap with the signal in intermediate or merger-ringdown stage in time domain, even though the blip glitch contributes excess power only to intermeidate and merger-ringdown frequency bands. Unlike the case with the tomte glitch, the blip glitch overlapping the signal at inspiral stage in time domain has no observable effect on parameterized tests of GR, since the posterior distribution matches with that with the glitch removed through low-passing, inpainting and deglitching. This may be due to the fact that the blip glitch did not strictly overlap with the signal tract in time-frequency space. However, with inspiral testing parameters introduced, the sampling of chirp mass is inaccurate, peaking around 5 $M_\odot$ greater than the injected value; this may be correlated to the deviation of $\delta\chi_4, \delta\chi_5^l, \delta\chi_6$ from the GR value of 0.

Comparing the unmitigated and mitigated results of the glitch overlapping the intermediate and merger-ringown stage in time domain, all three mitigation methods of low-passing, inpainting and deglitching can reduce false violations of GR, by bringing posteriors of testing parameters which excludes the GR value of 0 in the unmitigated case to a posterior that peaks close to 0 (e.g. $\delta\chi_3, \delta\chi_4, \delta\beta_2, \delta\beta_3, \delta\alpha_2, \delta\alpha_4$ in Fig. 7c). The posterior distribution of the testing parameters matches each other closely, indicating that the mitigation methods did not contribute extra effects on parameterized tests of GR in this three cases.

VI. CONCLUSION AND OUTLOOK

We reviewed a type of parameterized gravitational-wave tests of GR and the glitch mitigation methods of band-pass filtering, inpainting and glitch model subtraction using the `BayesWave` algorithm. We injected a high-mass-ratio coalescing BBH signal coherently into the LIGO-Hanford, LIGO-Livingston and Virgo detector output at times when long-duration low-frequency scattered-light glitches or short-duration broadband tomte and blip glitches are present in LIGO-Hanford or LIGO-Livingston. We then investigated the effect of the three type of glitches and their mitigations on parameterized tests of GR by comparing between unmitigated and mitigated results.

We showed that a tomte glitch, which contributes excess power to inspiral and intermediate frequency bands, lead to false violations in inspiral parameters; while a blip glitch, which contributes excess power to intermediate and merger-ringdown frequency bands, lead to false violations in parameters from all stages of coalescence. We found no clear correlation between the time of glitch-overlapping and the stages of coalescence which false violation occurred, except in one case where the signal and glitch did not overlap in time-frequency space, no obvious effects of the glitch can be observed.

Out of the three mitigation methods, we find that inpainting and `BayesWave` glitch model subtraction consistently reduces false violations of GR, and the results matches closely with each other. This indicates that the two methods did not introduce additional effects to parameterized tests, and suggests successful glitch removals. Band-pass filtering, on the other hand, can also reduce false violations in most cases. However, false violations are amplified or new violations are introduced

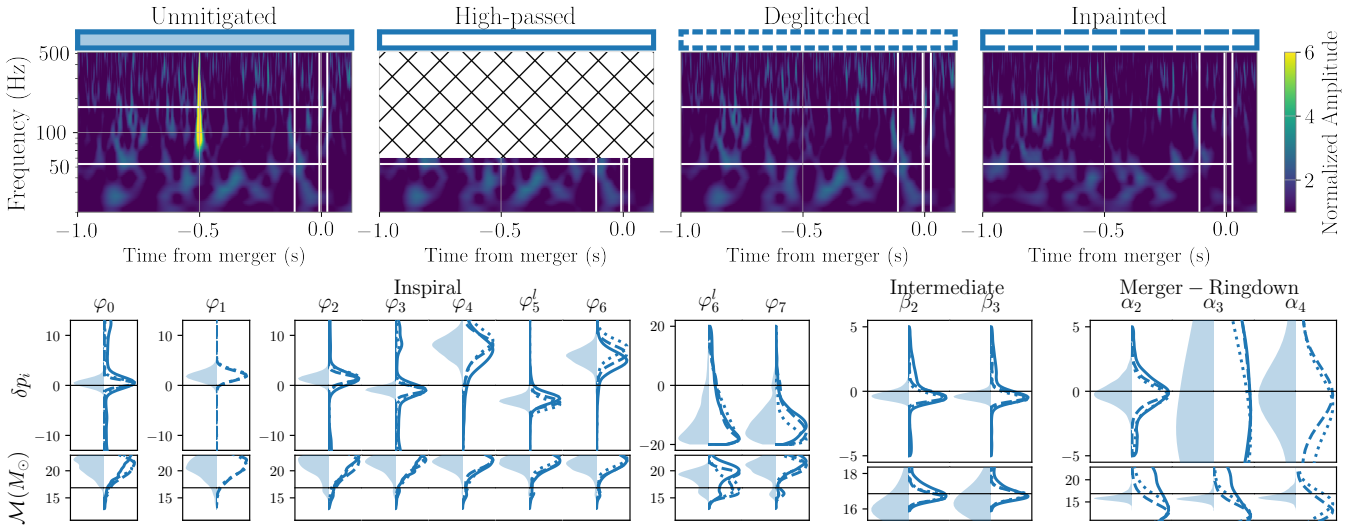

(a) Simulated GW190828_065509-like signal overlapped with a H1 blip glitch at inspiral stage in time domain.

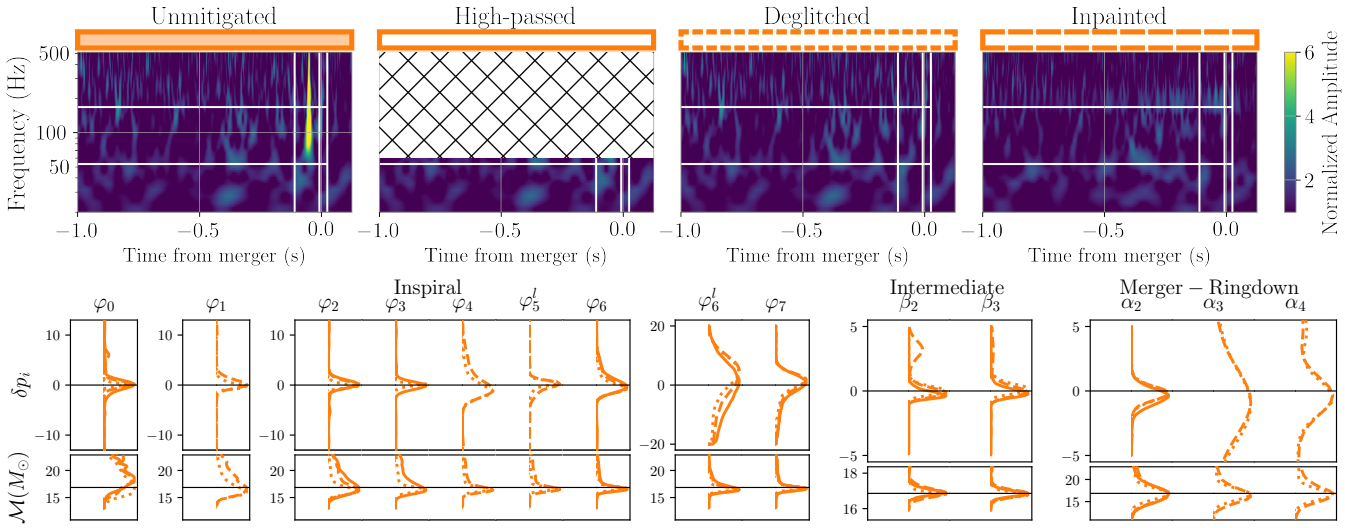

(b) Simulated GW190828_065509-like signal overlapped with a H1 blip glitch at intermediate stage in time domain.

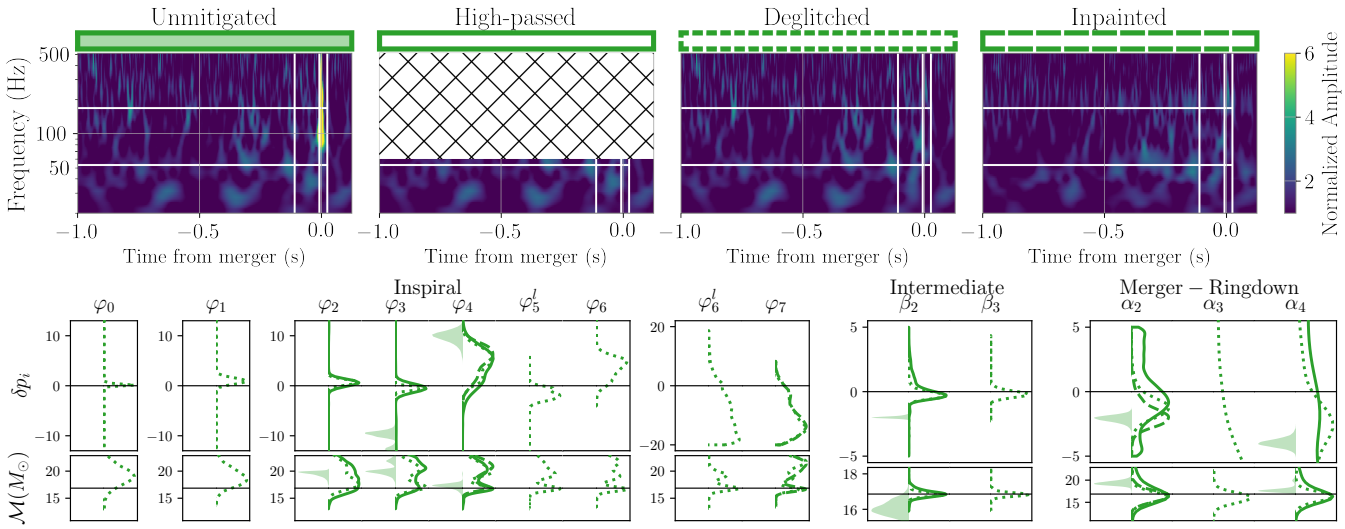

(c) Simulated GW190828_065509-like signal overlapped with a H1 blip glitch at merger-ringdown stage in time domain.

FIG. 7. Posterior distributions of testing parameters and the recovered chirp mass obtained by performing parameterized tests on unmitigated blip-glitch-overlapped signals during a three-detector observation (left of violin plot) and the corresponding mitigated cases (right of violin plot) where band-pass filtering (solid line), `BayesWave` glitch model subtraction (dotted line) and inpainting (dashed line) are performed. The GR-value of the testing parameters and the injected value of chirp mass are indicated by vertical black lines.

in more than one case after high-passing to 105 Hz. We suggest the application of inpainting or `BayesWave` glitch model subtraction for glitch mitigation, as they are found to be effective even when an extra degree of freedom is involved with the introduction of parameterized deviation to the signal model.

A major improvement on the LIGO detectors are expected to be completed in a few years, doubling the detector sensitivities [52]. The increased sensitivity in turn suggests more frequent occurrence of glitches overlapping signals. As mitigating glitch-overlapped signals may become a regularity in the future, a systematic study on the effects of glitches and their mitigation on parameter estimation and tests of GR will be crucial to the next generation of GW astronomy; this will be left for future work.

VII. ACKNOWLEDGMENTS

The author thanks Alan J. Weinstein and Rico K. L. Lo for providing instructive comments and reviewing the manuscript, Tjonnie G. F. Li for preparations before the LIGO SURF program, Derek Davis and Jonah Kanner for insightful discussions, Tyson Littenberg for providing the `BayesWave` glitch subtraction specifications. The author also thanks the National Science Foundation (NSF) and NSF REU for supporting the LIGO SURF program. Computing resources for this study was supported by the LIGO Laboratory and supported by the NSF Grants PHY-0757058 and PHY-0823459. LIGO was constructed by the California Institute of Technology and Massachusetts Institute of Technology with funding from the NSF and operates under cooperative agreement PHY-0757058. The LIGO SURF Program is supported by NSF award PHY-1852081. This report carries LIGO Document Number LIGO-T2000374.

[1] E. Berti, E. Barausse, V. Cardoso, L. Gualtieri, P. Pani, U. Sperhake, L. C. Stein, N. Wex, K. Yagi, T. Baker, *et al.*, *Testing general relativity with present and future astrophysical observations*, Classical and Quantum Gravity **32**, 243001 (2015), arXiv:1501.07274.

[2] C. W. Misner, K. S. Thorne, J. A. Wheeler, *et al.*, *Gravitation* (Macmillan, 1973).

[3] C. M. Will, *The Confrontation between General Relativity and Experiment*, Living Reviews in Relativity **9**, 3 (2006), arXiv:gr-qc/0510072 [gr-qc].

[4] C. M. Will, *The confrontation between general relativity and experiment*, Living reviews in relativity **17**, 4 (2014), arXiv:1403.7377 [gr-qc].

[5] K. Stelle, *Renormalization of higher-derivative quantum gravity*, Physical Review D **16**, 953 (1977).

[6] B. S. Sathyaprakash and B. F. Schutz, *Physics, Astrophysics and Cosmology with Gravitational Waves*, Living Reviews in Relativity **12**, 2 (2009), arXiv:0903.0338 [gr-qc].

[7] N. Yunes and X. Siemens, *Gravitational-wave tests of general relativity with ground-based detectors and pulsar-timing arrays*, Living Reviews in Relativity **16**, 9 (2013), arXiv:1304.3474 [gr-qc].

[8] N. Yunes, K. Yagi, and F. Pretorius, *Theoretical physics implications of the binary black-hole mergers gw150914 and gw151226*, Physical review D **94**, 084002 (2016), arXiv:1603.08955 [gr-qc].

[9] J. Meidam, K. W. Tsang, J. Goldstein, M. Agathos, A. Ghosh, C.-J. Haster, V. Raymond, A. Samajdar, P. Schmidt, R. Smith, *et al.*, *Parametrized tests of the strong-field dynamics of general relativity using gravitational wave signals from coalescing binary black holes: Fast likelihood calculations and sensitivity of the method*, Physical Review D **97**, 044033 (2018), arXiv:1712.08772 [gr-qc].

[10] E. Barausse, V. Cardoso, and P. Pani, *Can environmental effects spoil precision gravitational-wave astrophysics?*, Physical Review D **89**, 104059 (2014), arXiv:1404.7149 [gr-qc].

[11] J. Aasi, B. Abbott, R. Abbott, T. Abbott, M. Abernathy, K. Ackley, C. Adams, T. Adams, P. Addesso, R. Adhikari, *et al.*, *Advanced ligo*, Classical and quantum gravity **32**, 074001 (2015), arXiv:1411.4547 [gr-qc].

[12] F. Acernese, M. Agathos, K. Agatsuma, D. Aisa, N. Allemandou, A. Allocca, J. Amarni, P. Astone, G. Balestri, G. Ballardin, *et al.*, *Advanced virgo: a second-generation interferometric gravitational wave detector*, Classical and Quantum Gravity **32**, 024001 (2014), arXiv:1408.3978 [gr-qc].

[13] B. Abbott, R. Abbott, T. Abbott, S. Abraham, F. Acernese, K. Ackley, C. Adams, R. Adhikari, V. Adya, C. Affeldt, *et al.*, *Gwtc-1: a gravitational-wave transient catalog of compact binary mergers observed by ligo and virgo during the first and second observing runs*, Physical Review X **9**, 031040 (2019), arXiv:1811.12907 [astro-ph.HE].

[14] R. Abbott, T. Abbott, S. Abraham, F. Acernese, K. Ackley, A. Adams, C. Adams, R. Adhikari, V. Adya, C. Affeldt, *et al.*, *Gwtc-2: Compact binary coalescences observed by ligo and virgo during the first half of the third observing run*, arXiv preprint arXiv:2010.14527 (2020), arXiv:2010.14527 [gr-qc].

[15] B. P. Abbott, R. Abbott, T. D. Abbott, M. R. Abernathy, F. Acernese, K. Ackley, C. Adams, T. Adams, P. Addesso, R. X. Adhikari, *et al.*, *Tests of General Relativity with GW150914*, Phys. Rev. Lett. **116**, 221101 (2016), arXiv:1602.03841 [gr-qc].

[16] B. Abbott, R. Abbott, T. Abbott, S. Abraham, F. Acernese, K. Ackley, C. Adams, R. Adhikari, V. Adya, C. Affeldt, *et al.*, *Tests of general relativity with the binary black hole signals from the ligo-virgo catalog gwtc-1*, Physical Review D **100**, 104036 (2019), arXiv:1903.04467 [gr-qc].

[17] R. Abbott, T. Abbott, S. Abraham, F. Acernese, K. Ackley, A. Adams, C. Adams, R. Adhikari, V. Adya, C. Affeldt, *et al.*, *Tests of general relativity with binary black*

holes from the second ligo-virgo gravitational-wave transient catalog, arXiv preprint arXiv:2010.14529 (2020), arXiv:2010.14529 [gr-qc].
[18] P. R. Saulson, *Fundamentals of Interferometric Gravitational Wave Detectors* (2017).
[19] LIGO Scientific Collaboration, LIGO Algorithm Library - LALSuite, free software (GPL) (2018).
[20] J. Veitch, V. Raymond, B. Farr, W. Farr, P. Graff, S. Vitale, B. Aylott, K. Blackburn, N. Christensen, M. Coughlin, *et al.*, *Parameter estimation for compact binaries with ground-based gravitational-wave observations using the lalinference software library*, Physical Review D **91**, 042003 (2015), arXiv:1409.7215 [gr-qc].
[21] L. K. Nuttall, T. Massinger, J. Areeda, J. Betzwieser, S. Dwyer, A. Effler, R. Fisher, P. Fritschel, J. Kissel, A. Lundgren, *et al.*, *Improving the data quality of advanced ligo based on early engineering run results*, Classical and Quantum Gravity **32**, 245005 (2015), arXiv:1508.07316 [gr-qc].
[22] M. Zevin, S. Coughlin, S. Bahaadini, E. Besler, N. Rohani, S. Allen, M. Cabero, K. Crowston, A. K. Katsaggelos, S. L. Larson, *et al.*, *Gravity spy: integrating advanced ligo detector characterization, machine learning, and citizen science*, Classical and Quantum Gravity **34**, 064003 (2017), arXiv:1611.04596 [gr-qc].
[23] B. P. Abbott, R. Abbott, T. Abbott, M. Abernathy, F. Acernese, K. Ackley, M. Adamo, C. Adams, T. Adams, P. Addesso, *et al.*, *Characterization of transient noise in advanced ligo relevant to gravitational wave signal gw150914*, Classical and Quantum Gravity **33**, 134001 (2016), arXiv:1602.03844 [gr-qc].
[24] J. R. Smith, T. Abbott, E. Hirose, N. Leroy, D. MacLeod, J. McIver, P. Saulson, and P. Shawhan, *A hierarchical method for vetoing noise transients in gravitational-wave detectors*, Classical and Quantum Gravity **28**, 235005 (2011), arXiv:1107.2948 [gr-qc].
[25] T. Isogai, L. S. Collaboration, V. Collaboration, *et al.*, in *Journal of Physics: Conference Series*, Vol. 243 (IOP Publishing, 2010) p. 012005.
[26] R. Essick, L. Blackburn, and E. Katsavounidis, *Optimizing vetoes for gravitational-wave transient searches*, Classical and Quantum Gravity **30**, 155010 (2013), arXiv:1303.7159 [astro-ph.IM].
[27] R. Biswas, L. Blackburn, J. Cao, R. Essick, K. A. Hodge, E. Katsavounidis, K. Kim, Y.-M. Kim, E.-O. Le Bigot, C.-H. Lee, *et al.*, *Application of machine learning algorithms to the study of noise artifacts in gravitational-wave data*, Physical Review D **88**, 062003 (2013), arXiv:1303.6984 [astro-ph.IM].
[28] F. Robinet, N. Arnaud, N. Leroy, A. Lundgren, D. Macleod, and J. McIver, *Omicron: a tool to characterize transient noise in gravitational-wave detectors*, arXiv preprint arXiv:2007.11374 (2020), arXiv:2007.11374 [astro-ph.IM].
[29] C. Messick, K. Blackburn, P. Brady, P. Brockill, K. Cannon, R. Cariou, S. Caudill, S. J. Chamberlin, J. D. Creighton, R. Everett, *et al.*, *Analysis framework for the prompt discovery of compact binary mergers in gravitational-wave data*, Physical Review D **95**, 042001 (2017), arXiv:1604.04324 [astro-ph.IM].
[30] S. A. Usman, A. H. Nitz, I. W. Harry, C. M. Biwer, D. A. Brown, M. Cabero, C. D. Capano, T. Dal Canton, T. Dent, S. Fairhurst, *et al.*, *The pycbc search for gravitational waves from compact binary coalescence*, Classical and Quantum Gravity **33**, 215004 (2016), arXiv:1508.02357 [gr-qc].
[31] N. J. Cornish and T. B. Littenberg, *Bayeswave: Bayesian inference for gravitational wave bursts and instrument glitches*, Classical and Quantum Gravity **32**, 135012 (2015), arXiv:1410.3835 [gr-qc].
[32] T. B. Littenberg and N. J. Cornish, *Bayesian inference for spectral estimation of gravitational wave detector noise*, Phys. Rev. D **91**, 084034 (2015), arXiv:1410.3852 [gr-qc].
[33] B. Zackay, T. Venumadhav, J. Roulet, L. Dai, and M. Zaldarriaga, *Detecting gravitational waves in data with non-gaussian noise*, arXiv preprint (2019), arXiv:1908.05644 [astro-ph.IM].
[34] C. Pankow, K. Chatziioannou, E. A. Chase, T. B. Littenberg, M. Evans, J. McIver, N. J. Cornish, C.-J. Haster, J. Kanner, V. Raymond, *et al.*, *Mitigation of the instrumental noise transient in gravitational-wave data surrounding gw170817*, Physical Review D **98**, 084016 (2018), arXiv:1808.03619 [gr-qc].
[35] S. Chatterji, L. Blackburn, G. Martin, and E. Katsavounidis, *Multiresolution techniques for the detection of gravitational-wave bursts*, Classical and Quantum Gravity **21**, S1809 (2004), arXiv:gr-qc/0412119 [gr-qc].
[36] M. Hannam, P. Schmidt, A. Bohé, L. Haegel, S. Husa, F. Ohme, G. Pratten, and M. Pürrer, *Simple model of complete precessing black-hole-binary gravitational waveforms*, Physical review letters **113**, 151101 (2014), arXiv:1308.3271 [gr-qc].
[37] W. B. Davenport, W. L. Root, *et al.*, *An introduction to the theory of random signals and noise*, Vol. 159 (McGraw-Hill New York, 1958).
[38] J. D. Romano and N. J. Cornish, *Detection methods for stochastic gravitational-wave backgrounds: a unified treatment*, Living reviews in relativity **20**, 2 (2017), arXiv:1608.06889 [gr-qc].
[39] P. Whittle, *Hypothesis testing in time series analysis*, Vol. 4 (Almqvist & Wiksells boktr., 1951).
[40] S. Khan, K. Chatziioannou, M. Hannam, and F. Ohme, *Phenomenological model for the gravitational-wave signal from precessing binary black holes with two-spin effects*, Physical Review D **100**, 024059 (2019), arXiv:1809.10113 [gr-qc].
[41] S. Khan, S. Husa, M. Hannam, F. Ohme, M. Pürrer, X. J. Forteza, and A. Bohé, *Frequency-domain gravitational waves from nonprecessing black-hole binaries. ii. a phenomenological model for the advanced detector era*, Physical Review D **93**, 044007 (2016), arXiv:1508.07253 [gr-qc].
[42] S. Husa, S. Khan, M. Hannam, M. Pürrer, F. Ohme, X. J. Forteza, and A. Bohé, *Frequency-domain gravitational waves from nonprecessing black-hole binaries. i. new numerical waveforms and anatomy of the signal*, Physical Review D **93**, 044006 (2016), arXiv:1508.07250 [gr-qc].
[43] C. Cutler and E. E. Flanagan, *Gravitational waves from merging compact binaries: How accurately can one extract the binary's parameters from the inspiral waveform?*, Physical Review D **49**, 2658 (1994), arXiv:gr-qc/9402014 [gr-qc].
[44] F. J. Harris, *On the use of windows for harmonic analysis with the discrete fourier transform*, Proceedings of the IEEE **66**, 51 (1978).
[45] B. P. Abbott, R. Abbott, T. Abbott, F. Acernese, K. Ackley, C. Adams, T. Adams, P. Addesso, R. Ad-

hikari, V. Adya, *et al.*, *Gw170817: observation of gravitational waves from a binary neutron star inspiral*, Physical Review Letters **119**, 161101 (2017), arXiv:1710.05832 [gr-qc].
[46] B. P. Abbott, R. Abbott, T. D. Abbott, F. Acernese, K. Ackley, C. Adams, T. Adams, P. Addesso, R. X. Adhikari, V. B. Adya, *et al.*, *Multi-messenger observations of a binary neutron star merger*, The Astrophysical Journal **848**, L12 (2017), arXiv:1710.05833 [astro-ph.HE].
[47] J. McIver, M. Millhouse, G. Ashton, D. Davis, J. Veitch, and T. Littenberg, *O3a catalog mitigated data review results and status spreadsheet*, LIGO-T2000260 .
[48] Private communication with D. Davis.
[49] N. J. Cornish, T. B. Littenberg, B. Bécsy, K. Chatziioannou, J. A. Clark, S. Ghonge, and M. Millhouse, *The BayesWave analysis pipeline in the era of gravitational wave observations*, arXiv e-prints , arXiv:2011.09494 (2020), arXiv:2011.09494 [gr-qc].
[50] Private communication with Rico K. L. Lo.
[51] Calibrated, cleaned data from H1 and L1 are taken from the strain channel `DCS-CALIB_STRAIN_CLEAN_C01`. Reproduced data from V1 is taken from the strain channel `Hrec_hoft_V1O3Repro1A_16384Hz`.
[52] J. Miller, L. Barsotti, S. Vitale, P. Fritschel, M. Evans, and D. Sigg, *Prospects for doubling the range of advanced ligo*, Physical Review D **91**, 062005 (2015), arXiv:1410.5882 [gr-qc].